RSC Advances

PAPER

View Article Online
View Journal | View Issue

Cite this: *RSC Adv.*, 2022, **12**, 34584

Structural, optical, magnetic, and enhanced antibacterial properties of hydrothermally synthesized Sm-incorporating α-MoO_3 2D-layered nanoplates

Sapan Kumar Sen, *[a] M. Rajib Munshi,[b] Arup Kumar,[c] A. A. Mortuza, [a] M. S. Manir,[d] M. A. Islam,[e] M. N. Hossain[f] and M. Khalid Hossain *[a]

In this study, we have synthesized pristine and [0.5,1.5, and 2.5] M% samarium (Sm)-incorporating α-MoO_3 2D-layered nanoplates utilizing a facile hydrothermal process, and investigated the physical properties along with antibacterial effectiveness. X-ray diffraction (XRD) patterns confirmed the single-phase, stable orthorhombic polycrystalline structure of the as-prepared samples. The crystallite size, lattice strain, and dislocation density were measured using both Debye–Scherrer (D–S) and Williamson-Hall (W-H) techniques. Both pristine and Sm-incorporating α-MoO_3 samples showed two-dimensional (2D) layered nanoplate-type surface morphology, revealed by field emission scanning electron microscopy (FE-SEM) images. Energy dispersive X-ray spectroscopy (EDS) confirmed the presence of Sm contents in the α-MoO_3 matrix. After Sm incorporation in α-MoO_3, the different functional groups as well as vibrational groups were observed by Fourier-transform infrared (FTIR) spectroscopy and Raman spectroscopy analyses, respectively. The optical band gaps were measured from UV-vis diffuse reflectance spectroscopy (DRS) by employing the Kubelka–Munk formula and interestingly it is found that the bandgap energy (E_g) gradually decreased from 2.96 to 2.83 eV with the increment of Sm content. When compared to pristine α-MoO_3, the Sm-incorporating samples experienced a steady improvement in room temperature ferromagnetic (RTFM) behavior as Sm content increased, as measured by hysteresis loops. The antibacterial activities of both samples were assessed against Gram-positive: *Staphylococcus aureus* (*S. aureus*), and Gram-negative: *Escherichia coli* (*E. coli*) and *Salmonella enteritidis* (*S. enteritidis*) bacteria by the agar well diffusion method and enhanced antibacterial activity was observed as the Sm concentration increased, compared to pristine nanoplates. The obtained results suggest that the synthesized Sm-incorporating α-MoO_3 2D-layered nanoplate could be a potential antibacterial agent.

Received 24th August 2022
Accepted 24th November 2022

DOI: 10.1039/d2ra05304g

rsc.li/rsc-advances

1 Introduction

Because of the large influence on patient wellbeing and environmental safety issues, healthcare-associated (nosocomial) infections (HAIs) have been a serious worry among scientists in recent years due to rapidly rising death rates and increasing annual costs for HAI prevention.[1,2] The ubiquitous nature and ability of bacteria in the environment to grow, transfer, and develop multidrug resistance are significant challenges in this sector. A variety of detailed studies are required to produce new and effective antibacterial drugs to eliminate the ever-increasing concerns about bacterial infections. Nanotechnology, a new multidisciplinary discipline combining physics, chemistry, biology, and materials science, has enabled the most promising new insights to overcome the drawbacks of current antimicrobial treatments and the ongoing growth of bacterial resistance.

The increased interest in nanomaterials, particularly inorganic nanomaterials, for bioscience applications is due to their distinct features such as the high surface area to volume ratio, uniform size, shape, size distribution, morphology, surface functionalization, improved stability, and safety compared to organic antimicrobial agents.[3–7] Antimicrobial nanostructures offer a wide range of uses, including antibacterial textiles, catheter devices, biofilm suppression, and additions in paints

[a]*Institute of Electronics, Atomic Energy Research Establishment, Bangladesh Atomic Energy Commission, Dhaka 1349, Bangladesh. E-mail: sapansenphy181@gmail.com; khalid.baec@gmail.com; khalid@kyudai.jp*

[b]*Department of Physics, European University of Bangladesh, Dhaka 1216, Bangladesh*

[c]*Materials Science Division, Atomic Energy Centre, Bangladesh Atomic Energy Commission, Dhaka 1000, Bangladesh*

[d]*Institute of Radiation and Polymer Technology, Atomic Energy Research Establishment, Bangladesh Atomic Energy Commission, Dhaka 1349, Bangladesh*

[e]*Department of Physics, University of Barishal, Barishal 8200, Bangladesh*

[f]*Department of Glass & Ceramic Engineering, Bangladesh University of Engineering & Technology, Dhaka 1000, Bangladesh*

for antimicrobial surfaces, among others.[8] In the last few decades, antimicrobial characteristics of nanoparticles such as Ag, Au, Cu, ZnO, CuO, Fe_2O_3, TiO_2, CaO, Fe@Co_3O_4, MoS_2, and MgO have become an interesting area of investigation.[9–13] However, these oxide materials' limited active surface area, low durability, significant cytotoxicity in nature, and high costs limit their applicability as antibacterial devices. As a result, the scientific community faces a challenge in producing a new antibacterial agent using a low-cost nano-oxide material. Among several reported semiconductor nanomaterials, detailed studies of ZnO, CuO, Fe_2O_3, and TiO_2 have been reviewed and reported by several groups as compared to other materials as antimicrobial agents.[14–18]

Transition metal oxides (TMO) have recently received a lot of study attention due to their wide range of prospective applications in the emerging fields of photodetectors,[19] thin-film transistors,[20] photo-catalytic, optoelectronic, magneto-optic, photonic, gas sensors, transparent conductors, and photovoltaic solar cells, among others.[21–27] These materials can be used by incorporating transition metal (TM) ions into cation sites in host conventional semiconductors like MoO_3, ZnO, and TiO_2, and then introducing ferromagnetic properties into nonmagnetic semiconductors, allowing for simultaneous utilization of charge and spin carriers.[28–30] Moreover tuning the properties of various nanostructured materials like CdS, boron nitride (BN), PbS, and PbO have received attention for various applications.[31–33]

Molybdenum trioxide (MoO_3), in particular, among intrinsic n-type II–VI semiconductors, has a wide direct band gap of 2.8–3.2 eV at room temperature.[34] One of the most important and extensively studied TMO is MoO_3 because of its rich chemistry associated with multiple states, high thermal-chemical stability, suitable electronic, electrical, and optical properties, and numerous potential technological applications in the fields of spintronic devices, optoelectronic devices, magneto-optic devices, photonic devices, organic light-emitting diodes (OLEDs), charge injection or extraction layer in organic photovoltaic (OPVs), gas sensors, transparent conductors, photocatalytic, and photovoltaic solar cells.[35,36]

There are three basic crystal forms in MoO_3 material. The orthorhombic MoO_3 phase (α-MoO_3) is based on an octahedral MoO_6 basis, with all of the MoO_3 components sharing edges and corners, resulting in a zigzag chain and layered structure.[37] Whereas, there are two metastable MoO_3 phases namely monoclinic MoO_3 (β-MoO_3) and hexagonal MoO_3 (h-MoO_3) exist. It is necessary to modify the physical properties of MoO_3 nanoparticles to expand their applications in a variety of nanotechnology sectors, and this tuning may be accomplished *via* a variety of methods, including doping, annealing, and modifying production techniques.[38,39]

Doping, or the inclusion of a particular extrinsic element, is another straightforward, practical, and very effective method for altering and/or enhancing many properties of fundamental materials, such as electrical, magnetic, and optical capabilities.[40] Thus, as previously reported, the characteristics of MoO_3 may be altered by alloying it with a variety of elements such as cobalt (Co),[29] europium (Eu),[41] and dysprosium (Dy).[42] It is important to consider the radius of the dopant element since dopant atoms with comparable radii are recommended for producing compounds with minimum lattice imperfections.[42] Previously many research groups had replaced the small ionic radius Mo^{6+} (0.65 Å) with various larger ionic (0.74–0.97 Å) elements like Eu^{3+} (0.96 Å),[43] Cd^{2+} (0.97 Å),[44] Ce^{3+} (0.87 Å),[45] Dy^{3+} (0.91 Å),[46] Zn^{2+} (0.74 Å),[47] and Tb^{3+} (0.92 Å)[48] in order to get the desired properties for various applications. The benefit of doping metal oxides with rare earth metals such as Dy, Sm Ce, *etc.* is that the 4f empty orbitals make them easily mix with functional groups. Additionally, doping rare earth metals leads in an absorbance shift to the visible portion of the electromagnetic spectrum by manipulating structural parameters. As the rare-earth samarium ion (Sm^{3+}) has a radius of 1.08 Å, therefore, it would also be a good dopant for replacing the Mo ion (Mo^{6+}) in the MoO_3 lattice. Some recent reviews on rare-earth oxides and rare-earth elements as doping agents in various applications are also notable.[49–54] Another significant parameter affecting the quality of nanostructured materials is the annealing temperature. Several studies have been conducted on the influence of annealing temperature on unincorporated MoO_3 nanomaterials.[46,55]

The properties of generated nanostructures vary according to their size, shape, and many aspects such as synthesis processes. Thus far, unincorporated and incorporated nanostructured α-MoO_3 may be manufactured utilizing a variety of approaches, including hydrothermal synthesis, solution combustion synthesis, and probe ultrasonic synthesis, among others, to enhance the performance of these nanomaterials.[40,56] Each synthesis approach offers several distinct benefits over others. According to a review of the literature, the hydrothermal process is the most practical and effective method for modifying the size, shape, and other features of nanomaterials. Furthermore, the hydrothermal process is an enthralling, simple, affordable, and successful strategy.[43,57] However, the effects of Sm-incorporated in nanostructured α-MoO_3 synthesized by the hydrothermal method have not been explored so far.

In this work, nanostructured pristine α-MoO_3 and [0.5, 1.5, and 2.5 M%] Sm-incorporated α-MoO_3 were synthesized by a facile environment-friendly hydrothermal approach. The effect of Sm incorporation on the microstructural (lattice parameters, average crystallite size, crystalline nature, *etc.*), morphological, functional, Raman, optical and magnetic properties of the α-MoO_3 nanoplates are then investigated comprehensively using a variety of characterization techniques such as FE-SEM, XRD, EDX, FTIR, Raman spectroscopy, UV-vis spectroscopy, and a vibrating sample magnetometer (VSM) of a Quantum Design Physical Property Measurement System (PPMS). In addition, the antimicrobial activity of both samples was investigated against one Gram-positive (*S. aureus*) and two Gram-negative (*E. coli* and *S. enteritidis*) bacteria by the agar well diffusion method.

2 Experimental details

2.1 Materials

The ammonium heptamolybdate tetrahydrate (AHM), $(NH_4)_6Mo_7O_{24}\cdot 4H_2O$, was employed as the precursor material of Mo for the hydrothermal synthesis of pristine and [0.5, 1.5, 2.5] M%

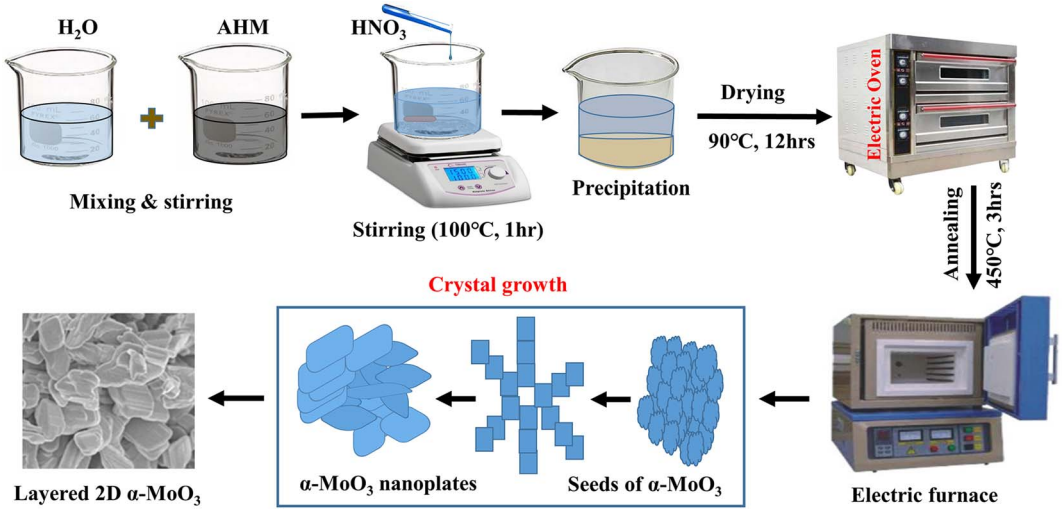

Fig. 1 The schematic diagram for the synthesis of pristine and Sm-incorporated α-MoO_3 nanoplates.

Sm-incorporated α-MoO_3 samples. Samarium(III) oxide (Sm_2O_3) was used as the source of the samarium. Other chemicals including concentrated nitric acid (37% HNO_3), de-ionized (DI) water, and ethanol were utilized in this process. All chemicals (Sigma Aldrich Ltd, USA) were analytical grades used without further purification.

2.2 Nanoplates preparation

To obtain a pure MoO_3 sample, 6 g of AHM was dissolved in 250 mL de-ionized (DI) water. The aqueous solution was magnetically stirred for 1 h at 75 rpm at room temperature. After that to achieve yellow precipitation, 24.5 mL of 37% HNO_3 was added drop by drop at 100 °C for 1 h using a hotplate with magnetic stirring. The precipitated MoO_3 was cleaned several times with ethanol and DI water. Following that, the washed MoO_3 was desiccated for 12 h at 90 °C in an electric oven to obtain MoO_3 nanopowders. Finally, the resulting MoO_3 nanopowder was annealed at 450 °C for 3 h in an electric furnace to obtain the final product of α-MoO_3 nanoplates. The above procedures were followed to obtain 0.5, 1.5, or 2.5 M% Sm-incorporated α-MoO_3 nanoplates. For this, the required amount of samarium(III) oxide (Sm_2O_3) was added with AHM. The possible chemical reaction to synthesize α-MoO_3 is given by eqn (1). In Fig. 1, the creation of α-MoO_3 nanoplates is depicted as well.

$$(NH_4)_6Mo_7O_{24}\cdot 4H_2O(aq) + 6HNO_3 \rightarrow 7MoO_3(s) + 6NH_4NO_3(aq) + 7H_2O(l) \quad (1)$$

2.3 Characterization

An X-ray diffractometer (3040-X'Pert PRO, Philips) was used to collect the X-ray diffraction (XRD) patterns of the pure and Sm-incorporated MoO_3 powder samples to evaluate phase purity and structural features. XRD analysis was performed using CuKα radiation of wavelength 1.54056 Å, where $2\theta = 10°$ to 70°, operating voltage = 40 kV, current = 30 mA, and scanning speed = 1° min^{-1}. An FE-SEM integrated with EDS (JEOL JSM-7600F) was utilized to investigate the surface morphologies along with elemental composition[58,59] of the synthesized samples, where the accelerating electric field was 5 kV. An FTIR (FTIR-ATR, Model: PerkinElmer Spectrum Two) with a scanning wavenumber range of 4000–400 cm^{-1} was used to identify the existing functional groups. A confocal Raman spectrometer (Monovista CRS+500) was used to obtain the Raman spectra with laser excitation at 532 nm. The optical investigation was carried out using a UV-vis DRS (Lambda 1050, PerkinElmer, USA) in the wavelength range of 250 to 800 nm. A vibrating sample magnetometer (VSM) of a Quantum Design PPMS was used to measure magnetic characteristics at room temperature.

2.4 Antibacterial testing of pristine and Sm-incorporated α-MoO_3 nanoplates

The antimicrobial effects of pristine and Sm-incorporated α-MoO_3 nanoplates against a Gram-positive bacterium, *Staphylococcus aureus* (ATCC 6538), and two Gram-negative bacteria, *Escherichia coli* (ATCC 8739) and *Salmonella enterica* (ATCC 14028) were analyzed using the agar well diffusion method with Mueller–Hilton Agar (MHA). Bacterial strains were cultured on Nutrient Agar media overnight at 37 °C. The bacterial colonies were suspended in 10 mL of sterile normal saline. Using UV-vis spectroscopy (Hitachi, Model: U-2910, Japan), the optical density (OD) was recorded at 580 nm and adjusted to achieve a cell density of 106–107 CFU mL^{-1} The good diffusion experiment was performed by pouring 25 mL of sterile MHA into Petri plates and allowing them to set. MHA plates were uniformly infected after solidification by swabbing test microorganisms with sterile cotton buds. Wells were bored into MHA plates after swabbing with a sterile borer (6 mm in diameter). Then, 100 µl of each concentration of 20 k, 40 k, 50 k, and 80 k ppm pristine and Sm-incorporated α-MoO_3 were added to each well. The plates were then incubated for 24 hours at 37 °C. To examine the antibacterial properties of both pristine and Sm-incorporated α-MoO_3, the zone of inhibition (ZOI) was measured in millimeters after incubation with a slide caliper.

3 Results and discussion

3.1 Structural properties

Fig. 2 demonstrates the XRD patterns of as-prepared pristine and [0.5, 1.5, 2.5] M% Sm-incorporated MoO_3 powder samples. The diffracted peaks at (020), (110), (040), (021), (111), (060), (002), and (081) planes are clearly distinguishable which are well-matched with the orthorhombic phase of MoO_3 (JCPDS # 05-0508) with space group *Pbnm* having $a = 3.962$ Å, $b = 13.858$ Å, $c = 3.697$ Å.[60] All samples show polycrystalline in nature. The sharp and well-defined peaks indicate a good crystalline structure and the absence of unwanted peaks confirms the phase purity of all samples. The most intense peak (021) at 27.28° of pristine α-MoO_3 is defined as the preferred orientation and no remarkable shifting was observed after the incorporation of Sm into the MoO_3 lattice. The lattice parameters determined from equation[61] are $a = 3.962$ Å, $b = 13.858$ Å, and $c = 3.697$ Å, which are in good agreement with the literature values and presented in Table 1. Using Debye Scherrer (D–S) equation (eqn (2)),[42] the crystallite size (D_{D-S}) is determined from the full width at half maximum (FWHM) values of the XRD peaks.

$$D_{D-S} = \frac{K\lambda}{\beta \cos\theta} \quad (2)$$

Where, D_{D-S}, λ, K, β, and θ signify the crystallite size, X-ray wavelength ($\lambda = 1.54056$ Å for CuKα), shape factor ($K = 0.90$), FWHM of the corresponding diffraction peak (in radian) positioned at 2θ, and Bragg angle (in degree), respectively. With the inclusion of Sm^{3+} atoms, the lattice strain (ε) and dislocation density (δ) develop in the α-MoO_3 lattice which can be determined from the Stokes–Wilson formula eqn (3) and eqn (4), respectively.[62]

$$\varepsilon = \frac{\beta}{4 \tan\theta} \quad (3)$$

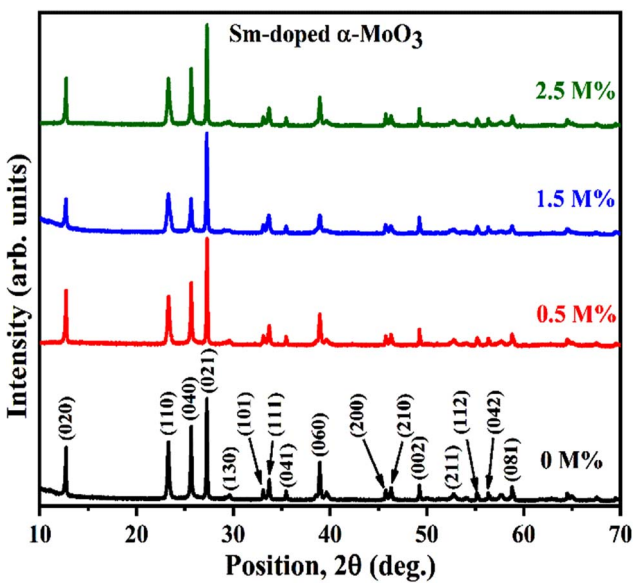

Fig. 2 XRD patterns of pristine and Sm-incorporated α-MoO_3 nanoplates.

Table 1 Lattice parameters (*a*, *b*, *c*) of pristine and Sm-incorporated α-MoO_3

	Lattice parameters		
Sample (M%)	*a* (Å)	*b* (Å)	*c* (Å)
0%	3.9675	13.9223	3.6981
0.5%	3.9633	13.9351	3.6981
1.5%	3.9638	13.9351	3.6983
2.5%	3.9642	13.9128	3.6975

$$\delta = \frac{1}{D^2} \quad (4)$$

Table 2 summarizes the estimated crystallite sizes, dislocation density, lattice strain, and other parameters. According to Table 2, the average crystallite sizes (D_{D-S}) considering all major peaks estimated from Debye–Scherrer formula is 44.8, 40.6, 35.8, and 39.8 nm for 0, 0.5, 1.5, and 2.5 M% Sm-incorporated α-MoO_3, respectively. The D_{D-S} value declined steadily from 44.8 to 35.8 nm up to 1.5 M% Sm, then increased slightly for 2.5 M% but was still lower than the pristine sample. As a result, the incorporated samples exhibited reduced crystallites. It's important to note that the corresponding dislocation density and strain values follow the reverse way of D_{D-S} assessed from Debye–Scherrer formula. To get more precise crystallographic properties, the Williamson-Hall (W-H) method is used.[63] The W-H approach is the most often employed method that takes into account size (Scherer) broadening (β_D), and strain broadening (β_S). Using this technique, eqn (5) represents the individual contribution to the broadening of reflection.

$$\beta = \beta_D + \beta_S \quad (5)$$

Applying the formula $\beta_D = \beta_D = \frac{k\,\lambda}{D\,\mathrm{Cos}\theta}$ and $\beta_S = 4\varepsilon\tan\theta$, one gets eqn (6).

$$\beta = \frac{k\,\lambda}{D\,\mathrm{Cos}\theta} + 4\varepsilon\,\tan\theta \quad (6)$$

The crystallite size, D_{WH} and lattice strain, ε_{WH}, are calculated using the following format (eqn (7)) of the above equation (eqn (6)):

$$\beta\,\mathrm{Cos}\theta = \frac{k\,\lambda}{D_{WH}} + 4\varepsilon_{WH}\sin\theta \quad (7)$$

The linear equation (eqn (7)) is known as the W-H equation. As illustrated in Fig. 3, the lattice strain (ε_{WH}) and crystallite size (D_{WH}) of pristine and Sm-incorporated α-MoO_3 can be estimated from the slope and *y*-intercept of linear fitted eqn (7), respectively. Using Fig. 3, the measured values of crystallite size (D_{WH}) are found to be 45.0, 41.5, 44.6, and 44.9 nm for 0, 0.5, 1.5, and 2.5 M% Sm-incorporated α-MoO_3, respectively. It can be noted that the reduction of D_{WH} as well as the increment of

Table 2 Structural parameters for pristine and Sm-incorporated α-MoO_3

	Debye–Scherer method			W-H method				
Sample (M%)	Strain, $\varepsilon \times 10^{-2}$	δ(lines per m^2) $\times 10^{14}$	D (nm)	Strain, $\varepsilon_{WH} \times 10^{-4}$	δ(lines per m^2) $\times 10^{14}$	D_{WH} (nm)	SF	Crystallinity (%)
0%	1.60	4.98	44.8	3.32	4.93	45.0	0.10	72.1%
0.5%	1.74	6.15	40.6	3.30	5.80	41.5	0.11	56.6%
1.5%	2.40	9.02	35.8	3.02	5.03	44.6	0.15	66.7%
2.5%	1.80	6.32	39.8	3.18	4.97	44.9	0.11	70.7%

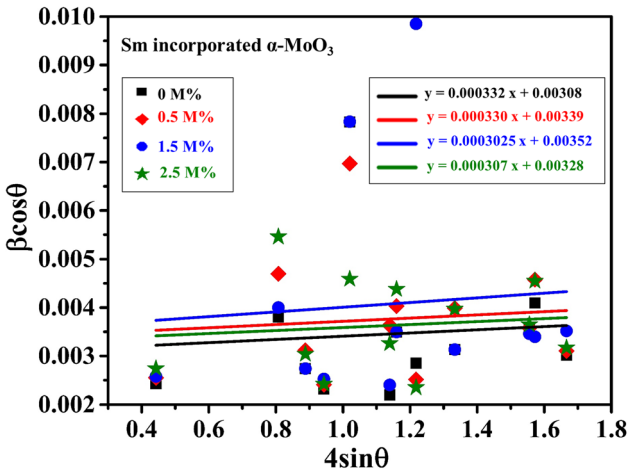

Fig. 3 W-H plot assuming UDM of 0.0, 0.5, 1.5, and 2.5 M% Sm-incorporated α-MoO_3.

ε_{WH} and δ resembles the Debye–Scherer trend. The varied nature of structural characteristics calculated using both methods are presented in Table 2 and the graphical representation is depicted in Fig. 4(a) and (b). According to calculated crystallite size values in both Debye–Scherrer and Williamson-Hall (W-H) formulae, a deterioration of crystallinity is observed as the crystallite size decreases from pristine to 1.5 M% Sm incorporated samples. The crystallite size is decreasing which might be the segregation of crystallites into smaller ones. In another way, the crystallite size decreases with increasing Sm amount, which may be attributed to the Sm cation interfering with the α-MoO_3 crystalline lattice. This interference effect could be attributable to the deformation of the crystal lattice caused by the larger ionic radius of Sm^{3+} (1.04 Å) compared to Mo^{6+} (0.74–0.97 Å). The lattice expands as the Sm concentration rises, which is also caused by the higher ion radius of Sm than that of Mo resulting in the declination of crystallinity.[64] Lattice strain is a measurement of the distribution of lattice constants brought on by crystal defects, particle size, dislocations, and oxygen vacancies, and more information regarding the number of crystal defects in the materials is revealed by the dislocation density. But for 2.5 M% Sm-incorporated α-MoO_3, the strain and dislocation density showed lower values and inversely crystallite size increased slightly. Here, it was expected to the movement of defects and atoms for a larger amount (2.5 M%) of Sm, and thus consequently, a larger cluster was formed due to the agglomeration of minute crystallites by crumbling the grain boundary that enhances the average crystallite size.[63] Some research groups reported a similar trend of change in crystallite size after doping. For example, Boukhachem *et al.*[7] investigated the Sn-doped MoO_3, and observed a considerable increase in crystallite size for 1 and 2 M% and then decreased for 3 and 4 M% Sn-doped MoO_3. Similarly, Al-Otaibi *et al.*[8] studied Zn-doped MoO_3 nanobelts and found that the crystallite size increased from 42.63 to 46.56 nm for 2 wt% Zn doping,

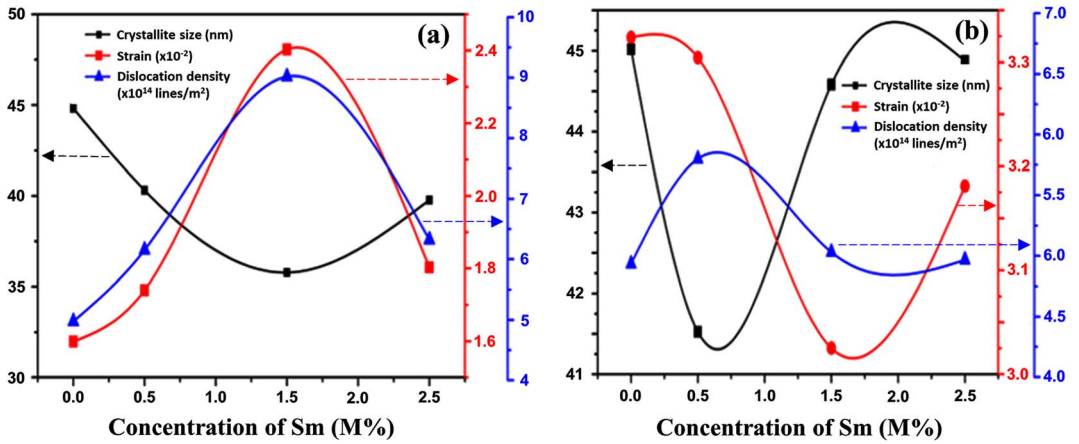

Fig. 4 Changes in strain, dislocation density, and crystallite size with Sm concentration variation in α-MoO_3 using (a) Debye–Scherer, and (b) Williamson-Hall methods.

decreased to 45.30 nm for 2.5 wt% Zn, increased to 51.98 nm for 3.3 wt% Zn, and finally decreased to 43.07 nm for 5 wt% Zn. The stacking fault indicates the crystal imperfections follow the decrement trend of ε_{WH} and δ. The crystallinity trended in the same manner as the crystallite size. The intensity and full width at half maximum (FWHM) of the XRD peaks are widely considered indicators of crystallinity and crystallite size.

3.2 Surface morphology and elemental analysis

Fig. 5(a)–(d) show the FE-SEM images of surface morphology of pristine and Sm-incorporated α-MoO_3 nanoplates. The multi-layered heap structure was clearly constructed from a two-dimensional (2D) nanoplate-like structure of α-MoO_3. To build these 2D layered α-MoO_3 structures, these layers are stacked in a staggered pattern and possibly held together by weak van der Waals forces.[65] In the FE-SEM micrographs shown in Fig. 5(a)–(d), the number of convolution layers ranges from three to forty-four. The thickness of a stack constructed with 44 layers is about 1 μm. A similar nanoplate morphology has been reported by various research groups.[66,67] The FE-SEM images of the doped and pristine α-MoO_3 samples show almost identical structures.

EDS has been used to determine the percentages of basic compositions present in the experimental samples. Fig. 6(a)–(d) show the EDS profile of pristine and doped MoO_3 nanoplates respectively. The elemental mass and atoms' presence is shown in Table 3. In Fig. 6(a) the EDS spectra peak at 0.525 keV and 2.36 keV confirm oxygen (O) and molybdenum (Mo), respectively. The atomic percentage shows the molar ratio of Mo : O is around 1 : 3 confirming the stoichiometry of MoO_3. The EDS peak at 2.36 keV in Fig. 6(b)–(d) shows the Sm-incorporation in α-MoO_3 nanoplates. As the atomic percentages of Sm increase with doping percentage variation are clearly in Table 3 confirmed that Sm was successfully incorporated into the α-MoO_3 matrix.

3.3 Functional properties

Functional groups have been identified at room temperature using Fourier transform inferred (FTIR) spectroscopy. Fig. 7 reveals the FTIR spectra of all samples in the wavenumber range of 400 to 4000 cm^{-1} (desired range 1000 to 450 cm^{-1}). All (pristine and Sm-incorporated) α-MoO_3 samples show three main characteristic vibrational bands of orthorhombic crystal structure (α-MoO_3) and no unwanted vibrational bands, confirming the chemical stability of the orthorhombic phase of as-synthesized materials after Sm incorporation and which results support the XRD examination. The two major vibrational zones (*i.e.*, 1000–600 cm^{-1} and 600–400 cm^{-1}) were observed in the spectra of all the samples. Four significant vibrational peaks are seen in the IR spectra of pristine α-MoO_3 nanoplates, located at 570.45, 812.88, 861.06, and 982.58 cm^{-1}, respectively; where a weaker peak is observed at 486.26 cm^{-1}. For pristine α-MoO_3,

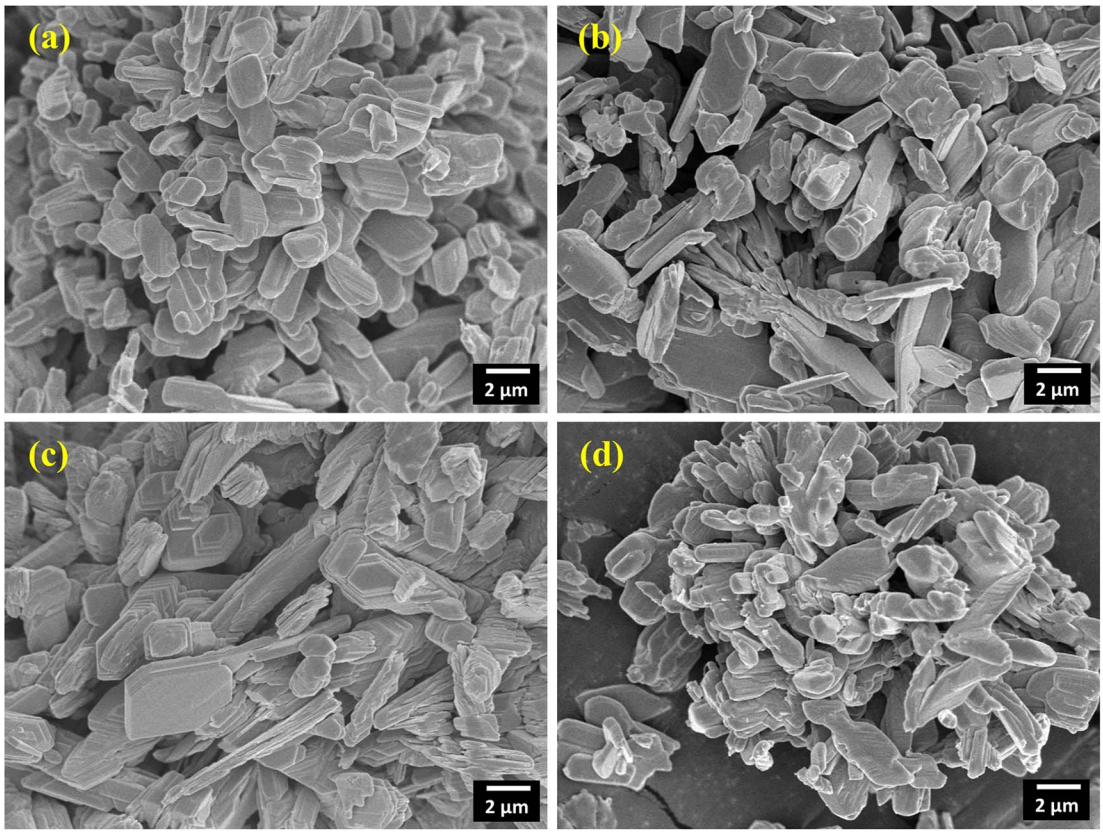

Fig. 5 2D layered nanoplate type micrographs of (a) pristine (b) 0.5 M%; (c) 1.5 M% and (d) 2.5 M% Sm-incorporated α-MoO_3.

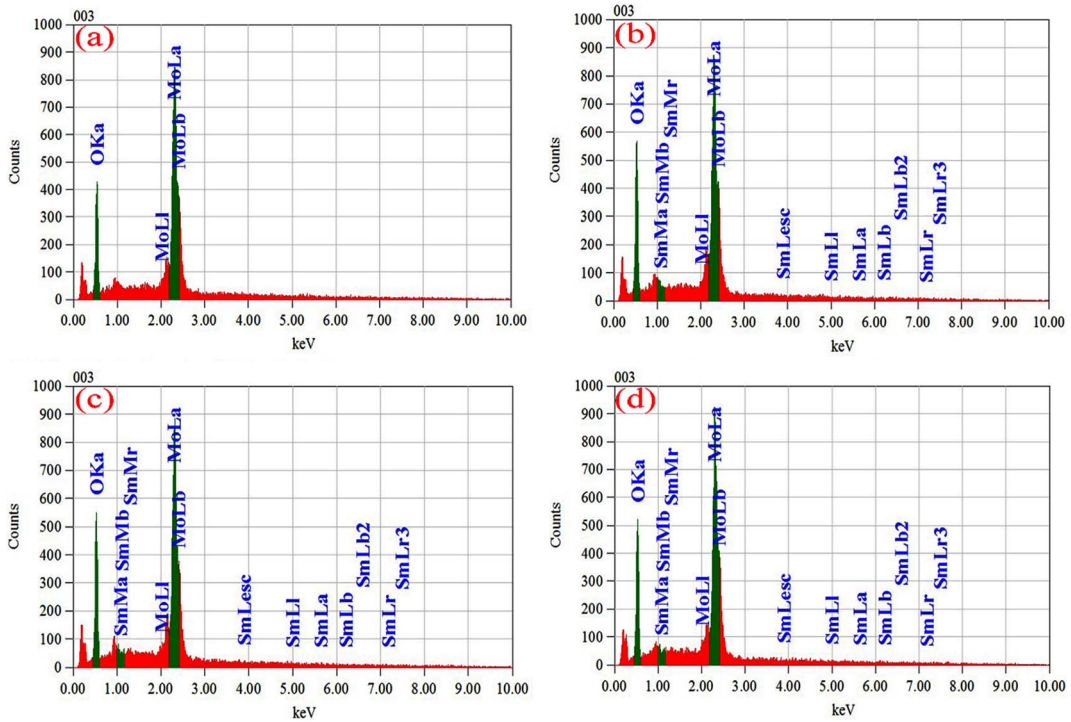

Fig. 6 EDX spectra of (a) pristine, (b) 0.5 M%, (c) 1.5 M%, (d) 2.5 M% Sm-incorporated α-MoO_3 nanoplate.

Table 3 The mass% and atom% of pristine and Sm-incorporated α-MoO_3

Sample	Elements	Mass%	Atom%
Pure α-MoO_3	O	37.40	78.18
	Mo	62.60	21.82
0.5% Sm-incorporated α-MoO_3	O	30.48	72.45
	Mo	68.67	27.26
	Sm	0.85	0.29
1.5% Sm-incorporated α-MoO_3	O	38.73	78.66
	Mo	60.15	20.89
	Sm	1.12	0.45
2.5% Sm-incorporated α-MoO_3	O	29.03	70.31
	Mo	69.27	28.96
	Sm	1.70	0.73

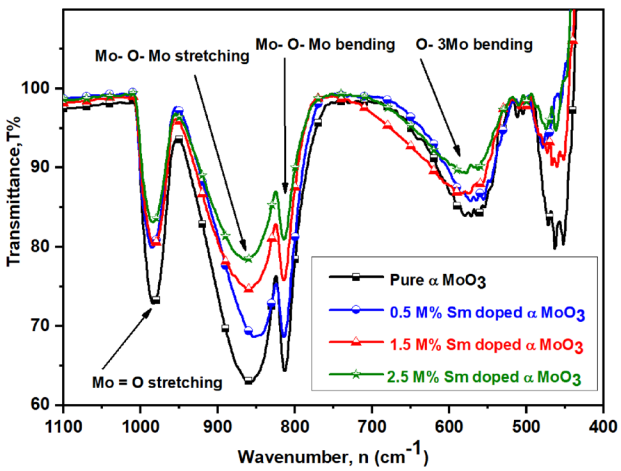

Fig. 7 FTIR spectra of pristine and Sm-incorporated α-MoO_3 nanoplates.

the sharp and intense peak at 982.58 cm^{-1} corresponds to the stretching vibration between oxygen and molybdenum atoms (Mo═O), which confirms the possible layered orthorhombic phase (α phase) or structure of MoO_3.[67–69] This band is found at 981.82, 981.82, and 983.48 cm^{-1} for 0.5, 1.5, and 2.5 M% Sm-incorporated α-MoO_3, respectively.

The pristine sample has a highly-intense signal at 861.06 cm^{-1}, which is attributed due to stretching vibrations of the bridge oxygen bond (O–Mo–O)[56] and is seen at 860.15, 861.82, 861.82 cm^{-1} for 0.5, 1.5, and 2.5 M% Sm-incorporated α-MoO_3, accordingly. Interestingly, it is clearly seen that the peak intensity of stretching vibration of $O_{(3)}$ atoms in the Mo–O–Mo units gradually decreased with rising Sm concentration in α-MoO_3 whereas almost no change in peak location is observed. A strongly sharp band is identified ascribed for Mo–O–Mo bending vibration located at the same position (812.88 cm^{-1}) of pristine and all Sm-incorporated α-MoO_3 samples although peak intensity sharply decreased with increasing Sm contents. The peak at 570.45 cm^{-1} is related to the bending vibrations of an oxygen atom ($O_{(2)}$) coupled to three metal atoms ν(O–3Mo) in pristine α-MoO_3 nanoplates[70,71] and this bending vibration can also be detected at 572.27, 573.18, and 576.67 cm^{-1} in 0.5, 1.5, and 2.5 M% Sm-incorporated α-MoO_3, respectively. A faint peak at 461.97 cm^{-1} is attributed to $Mo_{(2)}$–$O_{(4)}$ interaction with the water molecule and its strength declined as the Sm content increased.[72] Table 4 indicates the comparison of functional groups of α-MoO_3 nanoplates as a function of wavenumber

Table 4 Functional groups in pristine and (0.5, 1.5, and 2.5 M%) Sm-incorporated α-MoO_3

	Wavenumber, n (cm^{-1})			
Functional groups	0 M%	0.5 M%	1.5 M%	2.5 M%
Mo=O stretching vibration	982.58	981.82	981.82	983.48
Mo–O–Mo stretching vibration	861.06	860.15	861.82	861.82
Mo–O–Mo bending vibration	812.88	812.88	812.88	812.88
O–3Mo bending vibration	570.45	572.27	573.18	576.67

values after Sm incorporation. From the above discussion, it is clearly concluded that Sm contents affect the peak position and intensity of FTIR spectra of α-MoO_3 nanoplates without destroying the orthorhombic crystal structure.

3.4 Raman spectroscopy

In addition to the information provided by XRD patterns, Raman spectroscopy is an effective technique that can be used to investigate further changes in the phase formation, defect generation (oxygen vacancy), and microstructural parameters of the prepared nanocrystalline pristine and Sm-incorporated α-MoO_3 nanoplates due to Sm incorporation. Py and Maschke reported the Raman active phonon modes/characteristic Raman bands of the orthorhombic structure of molybdenum trioxide (space group: *Pbnm*) at 157 (A_g, B_{1g}), 195 (B_{2g}), 217 (A_g), 244 (B_{3g}), 287 (B_{2g}, B_{3g}), 295 (B_{3g}), 337 (B_{1g}, A_g), 375 (B_{1g}), 470 (A_g, B_{1g}), 666 (B_{2g}, B_{3g}), 819 (A_g, B_{1g}) and 995 (A_g, B_{1g}).[73] The room-temperature typical Raman spectra within the wavenumber range of 50–1100 cm^{-1} of pristine and Sm-incorporated α-MoO_3 nanoplates were collected using 632.8 nm excitation and are shown in Fig. 8. The positions (Raman shift) of the Raman vibrational bands and their corresponding active phonon modes are presented in Table 5. All of the detected Raman bands exhibit inappropriate positions that are very similar to those described in the nature of the orthorhombic layered structure of molybdenum trioxide (α-MoO_3) in the literature.[74] The characteristic bands of molybdenum trioxide in the 1050–600 and 500–100 cm^{-1} ranges are predominantly due to Mo–O stretching (ν_{as}) and bending (δ) modes, according to the vibrational analysis of Raman spectra as depicted in Fig. 8(b) and (c), respectively. The distinct, sharply intense peaks corresponding to molybdenum trioxide suggest that all α-MoO_3 have good crystallization.

The pristine samples exhibit Raman peaks at 132, 161, 201, 225, 251, 294, 343, 384, 477, 673, 825, and 1001 cm^{-1}, all of which are indicative of the α-MoO_3 phase.[74] The most intense peak positioned at 1001 cm^{-1} (A_g, B_{1g}) is ascribed due to the asymmetric stretch of the terminal oxygen atoms (ν_{as} Mo^{6+}=O) along the *a*- and *b*-axis of pristine α-MoO_3. This is the main characteristic vibrational mode of the α-phase.[41] The formation of oxygen vacancies should result in anion vacancies along the *c*-axis. As a result of the loss of bridging oxygen, the Mo atom is expected to shift towards the terminal oxygen in the b-direction, weakening the terminal bond along the *a*-axis.[41,76] The phonon mode observed at 825 cm^{-1} (A_g, B_{1g}) is assigned to the doubly coordinated oxygen (Mo–O–Mo) in the stretching mode of α-MoO_3.[77] Mo–O–Mo bridge is stretched asymmetrically along the *c* axis at 673 cm^{-1} (B_{2g}, B_{3g}). 343 and 384 cm^{-1} vibrational bands are attributed to δ (O–Mo–O) bending (B_{1g}, A_g) mode and δ (O–Mo–O) scissoring (B_{1g}) mode, respectively for pristine sample.[48] The peak at 294 and 251 cm^{-1} are due to the wagging mode of the terminal

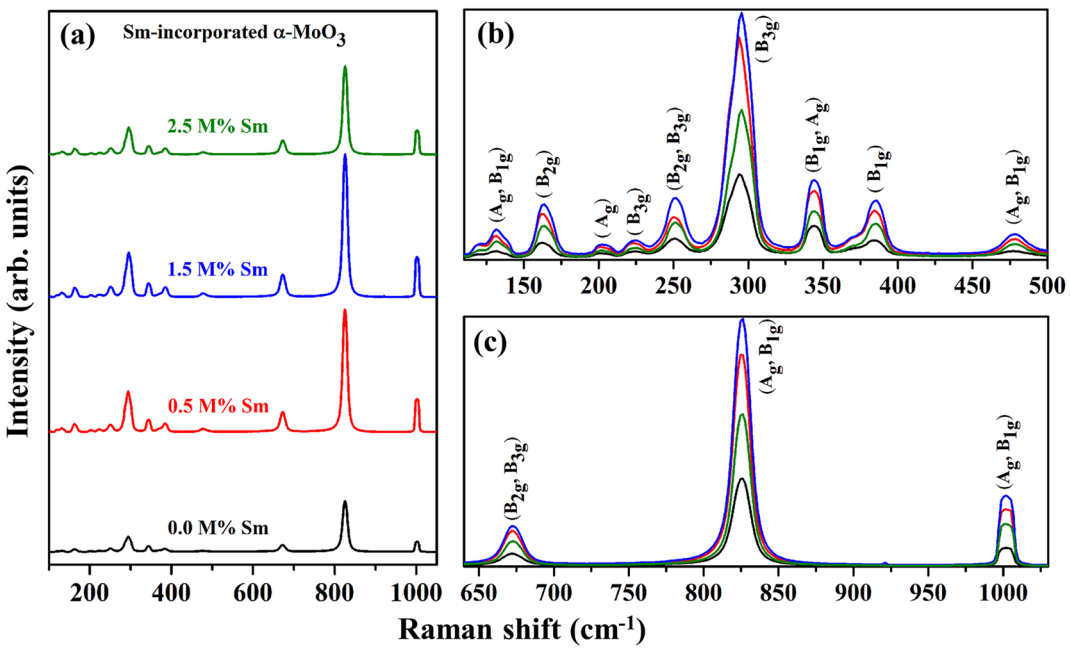

Fig. 8 Raman spectra (in the wavenumber range of (a) 100–1050 cm^{-1}, (b) 75–500 cm^{-1}, and (c) 640–1030 cm^{-1}) of (0.0, 0.5, 1.5, and 2.5 M%) Sm-incorporated α-MoO_3 nanoplates.

Table 5 Raman shift of active phonon modes in pristine and (0.5, 1.5, and 2.5 M%) Sm-incorporated α-MoO_3

Raman active phonon modes	Assignment	Raman shift (cm^{-1})				
		Standard (ref. 73,75)	0%	0.5%	1.5%	2.5%
(A_g, B_{1g})	Translational rigid MoO_4-chain mode, (T_b)	157	132	131	131	132
(B_{2g})	Twisting mode of the terminal oxygen, (τ O=M=O twist)	195	161	162	164	163
(A_g)	Rotational rigid MoO_4-chain mode, (R_c)	217	201	200	201	201
(B_{3g})	Twisting mode of the terminal oxygen, (τ O=M=O twist)	244	225	223	225	224
(B_{2g}, B_{3g})	Wagging modes of the terminal oxygen, (δ O=M=O waging)	287	251	250	251	251
(B_{3g})	δ O=M=O waging	295	294	293	295	294
(B_{1g}, A_g)	δ O–M–O bend	337	343	343	343	344
(B_{1g})	δ O=M=O scissor	375	384	383	385	385
(A_g, B_{1g})	ν_{as} O–M–O stretch and bend	470	477	477	479	477
(B_{2g}, B_{3g})	Asymmetric stretching of Mo–O–Mo bridge along the c axis, (ν_{as} O=M=O stretch)	666	673	682	673	677
(A_g, B_{1g})	Symmetric stretch of the terminal oxygen atoms, (ν_s O=M=O stretch)	819	825	822	831	826
(A_g, B_{1g})	Asymmetric stretch of the terminal oxygen atoms, (ν_{as} M=O) stretch	995	1001	1002	1002	1001

oxygen atoms, denoted as δ (O=M=O). Some low intense Raman peaks located at the lower Raman shift as a function of wavenumber value (Fig. 8(b)) at 132, 161, 201, 225, and 477 cm^{-1} originated due to the translational rigid MoO_4-chain mode (T_b) of (A_g, B_{1g}) symmetry, twisting mode of the terminal oxygen τ (O=M=O twist) of (B_{2g}), rotational rigid MoO_4-chain mode (R_c) of (A_g), twisting mode of the terminal oxygen τ (O = M=O twist) of (B_{3g}) and symmetric ν_{as} O–M–O stretching and bending vibration of (A_g, B_{1g}) mode, respectively.[78] There is no extra Raman peak due to the incorporation of Sm^{3+}, although the intensity of the phonon modes fluctuates with Sm admixing, indicating that Sm might only cause crystallographic defects and oxygen vacancies, not structural transformation.

3.5 Optical properties

Fig. 9(a) and (b) show the optical absorbance and reflectance spectra of pristine and Sm-incorporated α-MoO_3 nanoplates in the wavelength range 200–800 nm at room temperature utilizing UV-vis-NIR diffuse reflectance spectroscopy (DRS). Pristine and Sm-incorporated α-MoO_3 nanoplates exhibit high bandgap absorption in the UV spectra, as illustrated in Fig. 9(a) and (b). Absorption levels climb to peak values and then progressively decline over time in the visible range of the reflected light spectrum. An absorption band edge ranging from 375 to 425 nm was found in all samples, which may be due to the electronic bandgap transition. An explanation for the electronic bandgap transition is provided by the absorption of visible light by hybridized O-2p orbital with Mo 4d in the valence and conduction bands, respectively (which is mainly composed of Mo 4d orbital hybridized with O 2p).[79,80] Here, for the α-MoO_3 powder sample, Kubelka–Munk (K–M) function was utilized to estimate the optical bandgap (E_g) as follows (Eq. (8)).[63]

$$F(R) = (1 - R)^n/2R \quad (8)$$

As it is known to us, absorption co-efficient (α) is proportional relation to the K–M function, it can be written as eqn (9).

$$F(R) \propto \alpha = (h\nu - E_g)^n/h\nu \quad (9)$$

Where $F(R)$ is the Kubelka–Munk (K–M) function, R is the diffuse reflectance, α is the absorption coefficient, h is the plank's constant (6.626×10^{-34} J s), ν is light frequency, $h\nu$ is incident light energy, and E_g is the optical bandgap of the nanoplates. The presence of a straight line in the spectra indicates the optical bandgap of the as-synthesized nanoplates is of direct type. The characterization of the optical transition process is indicated by the factor n, and the value of n depends on the transition modes. n = 1/2, 2, 3/2, and 3 for direct allowed, indirect allowed, direct forbidden, and indirect forbidden modes, respectively.

The optical band gap energy of the corresponding materials is calculated by extrapolating the linear portion of the plot of $[F(R) \times h\nu]^2$ *versus* $h\nu$, and the tangent line with $[F(R) \times h\nu]^2 = 0$.[81] Fig. 10 shows that the direct bandgap energies (E_g) of pristine and 0.5, 1.5, and 2.5 M% Sm-incorporated α-MoO_3 nanoplates are found to be 2.96, 2.92, 2.89, and 2.83, respectively (Table 6). The bandgap energy is gradually reduced from 2.96 to 2.83 eV after incrementing of samarium contents up to 2.5 M%. Sm incorporation changes the optical characteristics vis-a-vis pristine α-MoO_3 nanoplates, as seen by the considerable shift of optical band gap energy into the visible region. It is generally

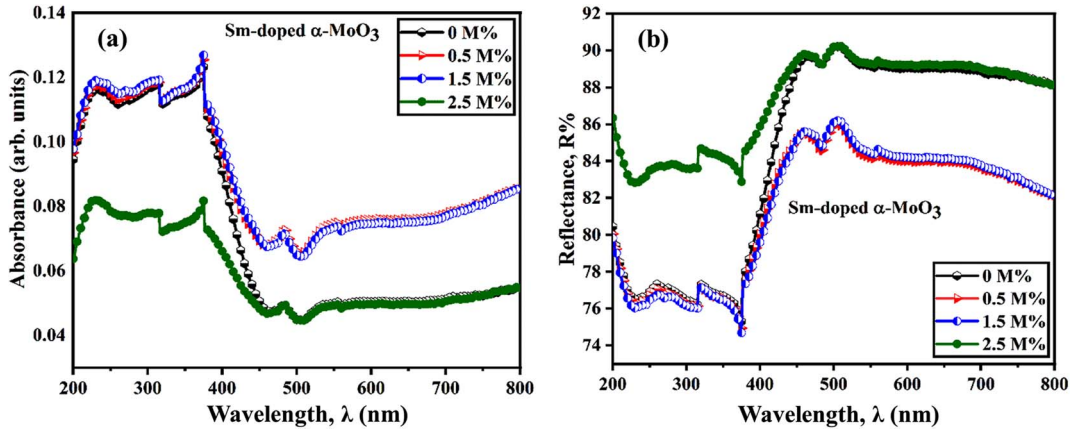

Fig. 9 (a) UV-vis absorbance spectra, and (b) UV-vis reflectance spectra derived from diffused reflectance spectroscopy of pristine and Sm-incorporated α-MoO_3 nanoplates, respectively.

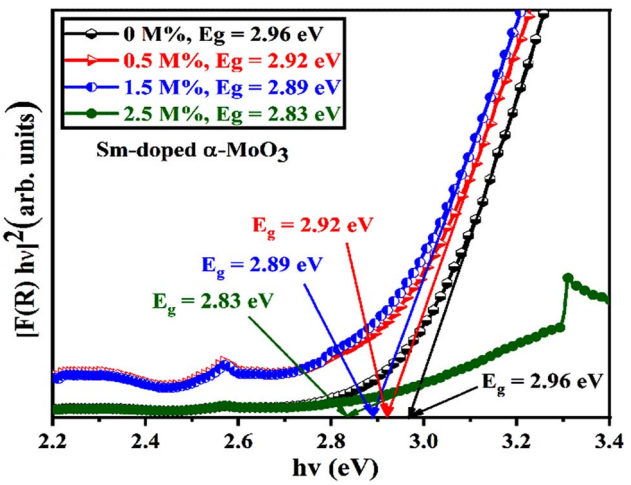

Fig. 10 $[F(R) \times h\nu]^2$ *vs.* incident photon energy, $h\nu$ plots to calculate bandgap energy of pristine and Sm incorporated α-MoO_3 nanoplates.

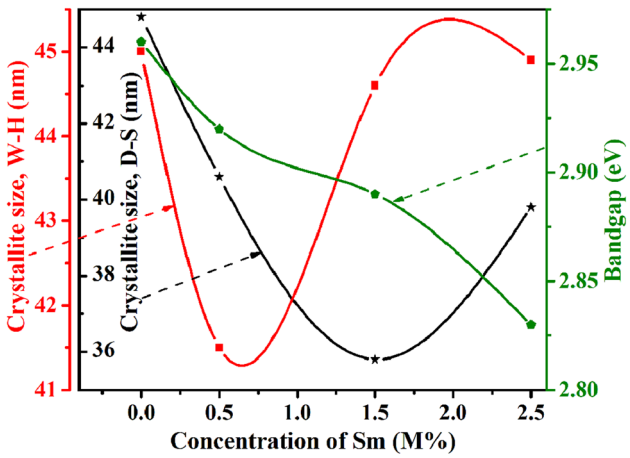

Fig. 11 Relation of crystallite size and bandgap with Sm concentration.

known that the value of E_g in bulk semiconductors is constant, but in nanostructured materials it can fluctuate according to the size of crystallites or crystal defects. The red shift trend of E_g values with increased Sm contents could be explained by the overall reduction of crystallite size caused by an increase in defects, disorders, and lattice strain, which is consistent with the findings of X-ray diffraction as shown in Fig. 11. When the Mo^{6+} ion in the MoO_3 matrix is replaced by Sm^{3+} ion, strain, defects, and charge imbalance might occur in the nanoplates. This may cause the valence band of incorporated nanoplates to broaden or the bandgap to narrow. In addition, the formation of sub-stoichiometric product,[82,83] as well as oxygen vacancies capable of capturing one or two electrons may contribute to the lowering of optical bandgap; the oxygen vacancies occupied by electrons act as donor centers. As a consequence, the impurity band is pushed farther into the forbidden gap region. Since the optical bandgap of the α-MoO_3 nanoplates has been reduced by substituting Sm^{3+} ions for Mo^{6+}, this may be the reason for this reduction. In the forbidden gap area, Sm^{3+} ions may create an impurity band.[84,85] Using Sm incorporation in α-MoO_3 to induce impurity levels suggests that a novel antibonding orbital has been discovered. There were two types of molecular orbitals: bonding and antibonding. The new antibonding orbital with lower energy provided unoccupied orbitals between the valence and conduction bands. There were changes in the valence and conduction bands due to oxygen vacancies as well as lattice instability, which reduced the bandgap.[78]

Table 6 Summary of the band gap energy, saturation magnetization (M_s), and coercivity (H_c) of the pristine and Sm-incorporated α-MoO_3

		Magnetic properties		
Sample (M%)	Band gap energy (eV)	Saturation magnetization, M_s(emu g^{-1})	Remanence, M_r (emu g^{-1})	Coercivity, H_c (kOe)
0%	2.96	0.0810	0.0100	0.1178
0.5%	2.92	0.3792	0.0292	0.0323
1.5%	2.89	0.3261	0.0121	0.0297
2.5%	2.83	0.3040	0.0190	0.0496

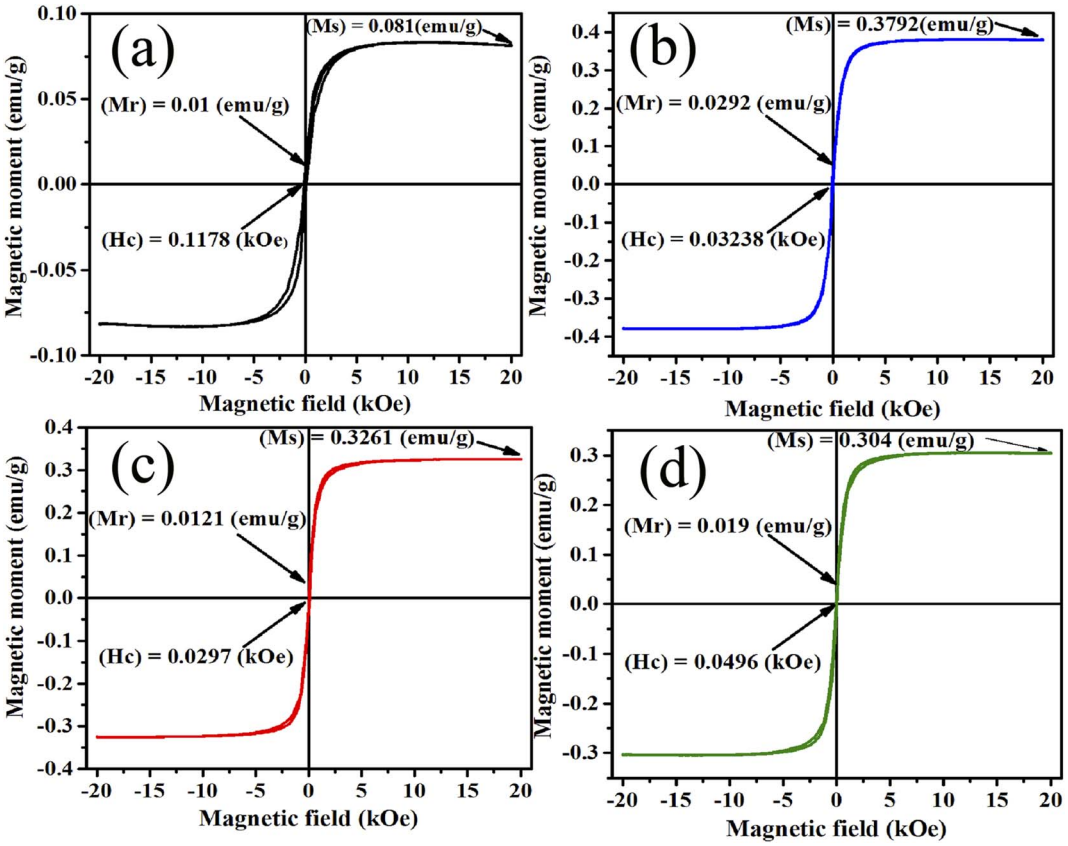

Fig. 12 *M*–*H* curve (a) 0% (b) 0.5% (c) 1.5% and (d) 2.5% Sm-incorporated α-MoO_3.

3.6 Magnetic properties

The PPMS technique was used to study the magnetic properties of pristine and samarium-incorporated 2D layered α-MoO_3 nanoplates. The behavior of magnetism of all samples was observed from the typical magnetization hysteresis (M–H) loops depicted in Fig. 12 by plotting the magnetic moment (M) against the applied magnetic field (H).[86] Magnetic properties such as saturation magnetization (M_s), remanence (M_r), and coercivity (H_c) of samples are listed in Table 6. All doped samples, including the pristine α-MoO_3 nanoplates, exhibited ferromagnetic hysteresis behaviors at room temperature. Similarly, the ferromagnetic nature of pristine α-MoO_3 was observed in several studies.[30,87] However, some previous reports also mentioned that the stoichiometric MoO_3 (bulk) is a paramagnetic semiconductor with no unpaired electron spins.[88,89]

In this experiment, the saturation magnetization (M_s) remarkably increased from 0.081 to 0.3792 emu g^{-1} after only 0.5% Sm incorporation in α-MoO_3 and remains high with increasing doping concentration. However, the coercivity (H_c) decreased with Sm incorporation. Because of oxygen vacancies, the ferromagnetic behavior observed in the pristine sample could be related to the non-stoichiometry composition found in MoO_3 nanoplates.[29] Ferromagnetic property enhanced after Sm incorporation may be due to (i) defect formation after doping in MoO_3 matrix, and (ii) generation of micro-cluster of Sm.[90] The relatively large radius of Sm increased strain in the MoO_3 matrix may lead to the segregation of Sm clusters in the doped sample. Raman and XRD studies show that the crystallinity has decreased; and the defects, oxygen vacancies, and faults increased with Sm doping concentration which clearly indicates the ferromagnetism enhancement at room temperature.

3.7 Antibacterial activity

Pristine and Sm-incorporated α-MoO_3 nanoplates were examined to determine their efficacy as a potential material for various biological uses, primarily as an antibacterial agent due to their lower toxicity. Fig. 13 shows the antimicrobial properties as a function of the zone of inhibition of pristine and Sm-incorporated α-MoO_3 nanoplates with varying concentrations against three bacteria. The images as a function of the inhibition zone seen in this figure are indicative of the results obtained after three repetitions of antimicrobial treatment of both nanoplate samples. According to the results, both nanomaterials are successful in producing a zone of inhibition against Gram-positive and Gram-negative bacterial strains, as depicted in Table 7. Nevertheless, Sm-incorporated α-MoO_3 nanoplates were found to be more active against the examined bacteria than pristine nanoplates.

In the context of pristine α-MoO_3 nanoplates, the largest zone of inhibition (16.68 mm in diameter) was recorded against *S. aureus* for the concentration of 80 000 ppm, which is good agreement with our previously reported largest zone of

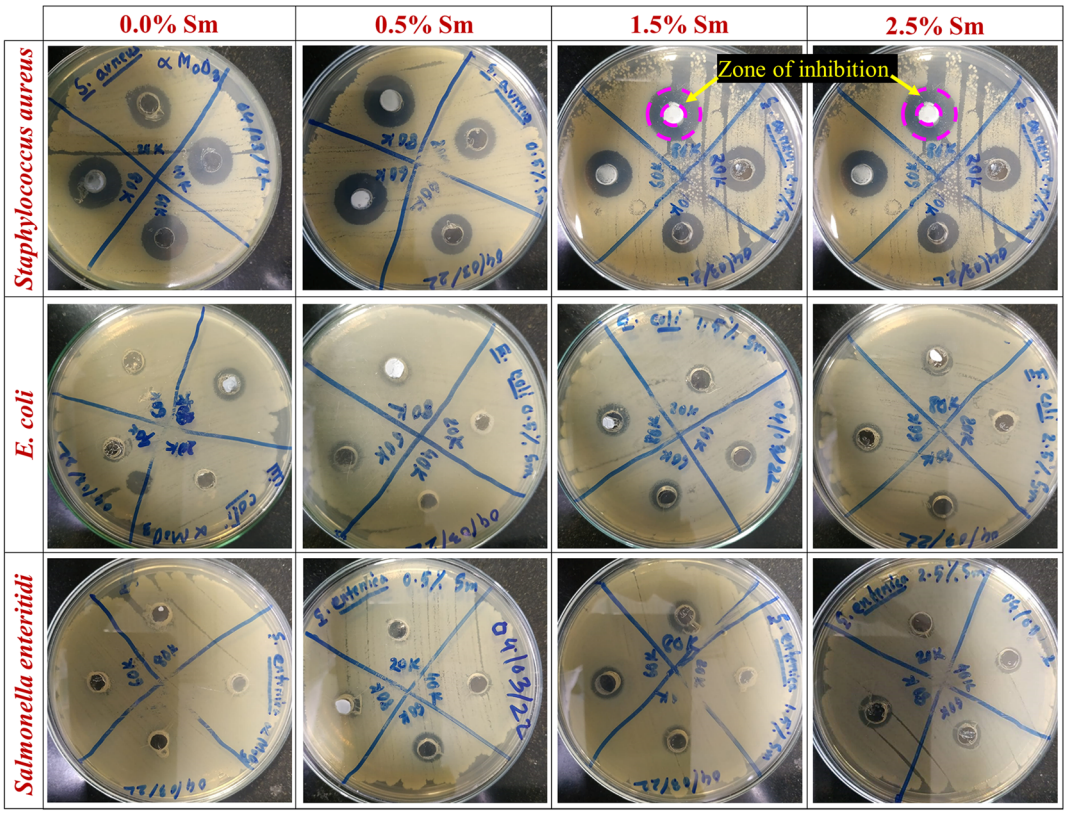

Fig. 13 Antibacterial activity of pristine and Sm-incorporated α-MoO_3 nanoplates against Gram-positive (*S. aureus*) and Gram-negative (*E. coli* and *S. enteritidis*) bacteria as a function of diameter (mm) of the zone of inhibition.

Table 7 Zone of inhibition (diameter in mm) caused by pristine and Sm-incorporated α-MoO_3 nanoplates

		Zone of inhibition (mm)			
Organisms	Conc. (ppm)	0.0% Sm	0.5% Sm	1.5% Sm	2.5% Sm
Staphylococcus aureus	20 000	12.56	13.47	11.25	14.74
	40 000	15.09	13.80	15.03	15.90
	60 000	15.61	17.12	16.15	16.21
	80 000	16.68	16.70	16.25	18.27
Escherichia coli	20 000	N/A	N/A	10.01	9.31
	40 000	10.51	N/A	10.96	10.21
	60 000	8.50	10.81	11.50	10.25
	80 000	11.45	10.87	11.52	10.29
Salmonella enteritidis	20 000	N/A	N/A	N/A	8.31
	40 000	8.34	9.01	9.71	8.76
	60 000	8.44	9.20	9.86	9.03
	80 000	9.03	9.33	9.91	10.35

inhibition for orthorhombic molybdenum trioxide nanoplates.[61] At a lower concentration (20 000 ppm), the pristine sample was inactive against both Gram-negative bacterial strains such as *E. coli* and *S. enteritidis*, and no zone was identified in Petri plates. Therefore, the ZOI of bared α-MoO_3 linearly depends on concentration and after increasing the concentration of molybdenum trioxide, its ZOI increased up to 11.45 and 9.03 mm for *E. coli* and *S. enteritidis*, respectively.

The antibacterial activity of α-MoO_3 nanoplates showed its increased value of ZOI due to 0.5% Sm admixing against all examined bacteria and the observed highest ZOI is (17.12 mm) against *S. aureus* at the concentration of 80 000 ppm. Although, no ZOI was found at comparatively lower concentrations against *E. coli* (20 000 and 40 000 ppm) and *S. enteritidis* (20 000 ppm) for 0.5% Sm. Similar enhanced inhibiting bacterial growth or killing bacterial cells (highest 17.25 mm, against *S. aureus* at 80 000 ppm) was identified for 1.5% Sm-incorporated α-MoO_3

nanoplates. From Fig. 13 and Table 7, it is clearly seen that the highest ZOI (18.27 mm) was determined against *S. aureus* at the concentration of 80 000 ppm for 2.5% Sm compared to other samples. As a result, these findings suggest the enhanced antibacterial effectiveness of α-MoO_3 nanoplates due to samarium incorporation in the α-MoO_3 matrix. It has been revealed that Sm-doped α-MoO_3 nanoplates are highly effective and that the growth of bacteria is inhibited when concentrations of Sm-doped α-MoO_3 nanoplates rise.

Understanding the interaction between the pure orthorhombic phase of MoO_3 nanomaterials and bacterial cell walls, which results in cell wall degradation, is a crucial one.[91] Several studies have suggested that the antibacterial properties of various nanomaterials are highly influenced by their morphologies (crystallite size and shape), crystallographic structure, surface defects, and composition of nanomaterials.[2,9,92–94]

In the case of metal oxide semiconductor nanomaterials, suitable doping element also plays a vital role in antimicrobial applications.[95,96] Chandar *et al.* reported that the incorporation of the Ni element in the MoO_3 matrix enhanced the antibacterial activity of MoO_3 nanomaterials compared to the undoped sample.[97] Ag also increased the effectiveness of MoO_3 against bacterial strains, explored by Raj *et al.*[95] Among various dopant elements, samarium is considered a less toxic and good one for enhancing the physical properties of transition metal oxides in the case of biological and other relevant applications.[96] As a result, samarium doping may improve the antimicrobial activity of α-MoO_3 nanoplates. The experimental results of the antibacterial activity of doped MoO_3 nanomaterials compared with previous reports are shown in Table 8.

The antimicrobial activity of the Sm doped α-MoO_3 nanoplates can be explained by three main mechanisms namely: (a) production of enhanced levels of reactive oxygen species (ROS)[98] on the surface of α-MoO_3 nanoplates, (b) release of Mo^{6+} ions from the α-MoO_3 nanoplates, and (c) size of the nanomaterials.[96,97,99] Fig. 13 clearly reveals inhibitory zones against bacterial strains, indicating that the Sm-doped α-MoO_3 nanoplates have damaged the bacteria's membrane wall. Bacteria are destroyed when oxygen species are released from the surface of Sm-incorporated α-MoO_3 nanoplates. Tables 2 and 7 show that the reduction in crystallite size of the Sm-incorporated α-MoO_3 nanoplates increased the size of the inhibitory zone resulting in increased surface area to volume ratio and formation of more H_2O_2.[95] The interstitial occupancy of the Sm-incorporated α-MoO_3 lattice structure increased as the percentage of Sm increased, resulting in free carriers in the α-MoO_3 lattice. The free carriers play a crucial role in antibacterial effectiveness. The antibacterial efficiency as a function of ZOI of examined Sm-incorporated α-MoO_3 nanoplate samples is inversely propositional to crystallite size and linearly proportional to the surface area to volume ratio. Thus, the crystallite size of Sm-incorporated α-MoO_3 2D layered type nanoplate orthorhombic structure has a significant impact on activity most likely due to a large number of nanomaterials with oxygen species accumulating in the cell membrane.

The substitution of Sm ions (Sm^{3+}) into the Mo positions leads to a larger amount of Mo interstitials, causing more molybdenum ions to be released into the system. Interstitial Mo^{6+} ions are expected to have a higher chance of breaking out from the α-MoO_3 lattice. The liberated Mo^{6+} ions may have a strong electrostatic interaction with bacterial cell membranes, causing significant bacterial cell destruction. Therefore, the formation of Mo^{6+} ions is also one of the causes of the enhancement of antimicrobial activities of Sm-incorporated α-MoO_3 nanoplates. Furthermore, Sm ions (Sm^{3+}) contribute to damage to the bacterial cell membranes.

Basically, the antibacterial activity of Sm-incorporated α-MoO_3 2D layered nanoplates can be explained by the photocatalysis process under UV-vis irradiation depending on two mechanisms. Firstly, the physical process in which disruption of the bacterial membrane occurs by rupturing the potential and integrity due to surface interactions between the cell wall and nanoplates. Secondly, the chemical process includes the production of enhanced levels of ROS such as superoxide anion radical ($*O_2^-$), hydroxyl radical (*OH), and hydrogen peroxide radicals ($*H_2O_2$). The capacity of Sm-incorporated α-MoO_3 nanoplates to generate ROS is the primary cause for their improved antibacterial activity. Generally, many transition metal oxides are sportive against micro-organisms due to the interaction of hydrophobic and electrostatic forces.[100] The production of enhanced levels of these ROS can be explained as follows:[96,97,99] when 2D layered nanoplates of pristine and Sm-incorporated α-MoO_3 are exposed to light with the energy of photon equal to or higher than the energy bandgap of the α-MoO_3 semiconductor, electrons from the valence band (VB) are transferred to the conduction band (CB), leaving holes in the

Table 8 Comparative assessment of antibacterial activity (highest ZOI) of doped MoO_3 with earlier reports

Sl. no.	Materials	Dopant	Bacteria	Zone of inhibition (mm)		Ref.
				Pure	Doped	
1	h-MoO_3 nanorods	Ag	*B. cereus*	12 ± 0.4	07 ± 0.9	95
			C. koseri	16 ± 0.7	22 ± 0.5	
			P. aeruginosa	17 ± 0.3	23 ± 0.4	
2	α-MoO_3 nanorods	Ni	*E.coli*	16 ± 0.5	18 ± 0.5	97
			S. aureus	16 ± 1	19 ± 0.5	
3	α-MoO_3 nanoplates	Sm	*S. aureus*	16.68	18.27	Present
			E. coli	11.45	10.29	
			S. enteritidis	9.03	10.35	

valence band (eqn (10)). These excited electrons (e^-) in the CB can be trapped by the oxygen molecules (O_2) present on the surface, producing superoxide anion radicals ($*O_2^-$) (eqn (11)). Simultaneously, the holes (h^+) in the VB reacts with the water molecules (H_2O), emitting hydroxyl ion (OH^-) and hydrogen ion (H^+) (eqn (12)). The superoxide anion radicals ($*O_2^-$) thereafter interacts with H^+ to produce hydroperoxyl radical ($*HO_2$) (eqn (13)). The hydroperoxyl radical ($*HO_2$) combines with e^- and H^+ once more, resulting in hydrogen peroxide radical ($*H_2O_2$) (eqn (14)). At the same time, hydrogen peroxide radical ($*H_2O_2$) can react with superoxide anion radicals ($*O_2^-$) to generate hydroxyl radical (*OH), hydroxyl ion (OH^-) and singlet oxygen ($^1O_2$) (eqn (15)). The reactions that occur in this mechanism are illustrated in the following eqn (10–15):

$$MoO_3 + hn(\text{photon}) \rightarrow h^+(\text{hole}) + e^-(\text{excited electron}) + Mo^{6+} \quad (10)$$

$$e^-(\text{excited electron}) + O_2(\text{surface oxygen molecule}) \rightarrow *O_2^-(\text{superoxide anion radical}) \quad (11)$$

$$h^+(\text{hole}) + H_2O(\text{water molecule}) \rightarrow OH^- + H^+ \quad (12)$$

$$*O_2^-(\text{superoxide anion radical}) + H^+ \rightarrow *HO_2(\text{hydroperoxyl radical}) \quad (13)$$

$$*HO_2(\text{hydroperoxyl radical}) + e^-(\text{excited electron}) + H^+ \rightarrow *H_2O_2(\text{hydrogen peroxide radical}) \quad (14)$$

$$*H_2O_2(\text{hydrogen peroxide radical}) + *O_2^-(\text{superoxide anion radical}) \rightarrow *OH(\text{hydroxyl radical}) + O_2\ (\text{singlet oxygen}) + OH^-(\text{hydroxyl ion}) \quad (15)$$

The electron–hole pairs serve as the primary unit for the generation of ROS. The gradually decreasing optical band gap (from 2.96 to 2.83 eV) accelerates this ROS-producing mechanism by creating more electron–hole pairs as the Sm admixing level increases in the α-MoO_3 semiconductor. The negatively charged radicals (hydroxyl radicals and superoxide anions) cannot penetrate the cell membrane of micro-organisms, but they can induce critical damage to the bacteria's outer surface, whereas positively charged hydrogen peroxide radicals ($*H_2O_2$) can penetrate easily through the negatively charged bacterial cell membranes and kill the bacteria. Therefore, hydrogen peroxide radical ($*H_2O_2$) is highly harmful to damaging bacterial cell membranes. Further, the superoxide dismutase (SOD) mimetic/catalase assay analysis would be helpful to understand the levels of ROS with the incorporation of Sm. The detailed mechanism of SOD and catalase mimic activities of MoO_3-based materials like MoO_{3-x} nanodots were explained by Han *et al.*[101] It is worth noting that when the Sm level was increased up to 2.5 M%, in the α-MoO_3 semiconductor, the antibacterial efficiency against all three micro-organisms was found to be higher than that of the pristine. In this experiment, the improved antibacterial activity of α-MoO_3 nanoplates after Sm-incorporation is due to the following factors: decreased crystallite sizes, formation of defects and oxygen vacancies, two-dimensional plate type layered shape, improved ferromagnetic behavior, sinking optical band gap, increased levels of ROS, and (Mo^{6+} and Sm^{3+}) ions formation from the α-MoO_3 nanoplates.

4 Summary

Here, we have reported the impact of Sm contents on the physical properties and antibacterial activity of hydrothermally synthesized α-MoO_3 nanoplates. The single-phase orthorhombic structure with the polycrystalline nature was revealed by XRD patterns, supported by FTIR and Raman results. The overall crystallite size decreased with the increment of Sm contents, resulting in an increment of defects, strain, and dislocation density. The EDX spectra confirmed the Sm incorporation and the plate-type 2D layered shape was identified from the FE-SEM micrograph. The bandgap energy decreased gradually from 2.96 to 2.83 eV as the Sm content increased. The measured magnetic hysteresis loops lead to the ferromagnetic behavior of α-MoO_3 nanoplates. The room temperature ferromagnetism of 2.5 M% Sm α-MoO_3 increased compared to the pristine sample which is attributed to the existence of a large number of oxygen vacancies, supported by Raman studies as well. In comparison to the pristine one, the antibacterial activity enhanced as Sm contents increased in both Gram-positive (*S. aureus*) and Gram-negative (*E. coli* and *S. enteritidis*) bacteria. The reason might cause the decreased crystallite sizes, formation of defects and oxygen vacancies, 2D plate type layered morphology, enhanced ferromagnetic behavior, lowering optical band gap, enhanced levels of ROS, and (Mo^{6+} and Sm^{3+}) ions formation in the α-MoO_3 nanoplates. The investigated opto-structural and magnetic properties suggested that the synthesized Sm-incorporated 2D layered α-MoO_3 nanoplates might be suitable for photocatalysts, magneto-optic, and spintronic nanodevice applications. The enhanced antibacterial activity postulated that Sm-incorporated 2D layered α-MoO_3 nanoplates could be an innovative antibacterial approach for eradicating microorganisms in medicinal as well as public health sectors.

Data availability

All data used to evaluate the conclusion of this study are presented in the manuscript. Additional data can be available from the corresponding authors upon reasonable request.

Author's contributions

S. K. Sen: conceptualization, methodology, software, validation, formal analysis, investigation, data curation, writing – original draft, writing – review & editing, supervision, project administration; M. R. Munshi: software, writing – original draft; A. Kumar: investigation, data curation; A. A. Mortuza: writing – review & editing, software; M. S. Manir: resources, investigation, data curation; M. A. Islam: writing – review & editing; M. N. Hussain: data curation; M. K. Hossain: software, visualization; validation, writing – review & editing.

Conflicts of interest

The authors declare that they have no competing interests.

Acknowledgements

This research did not receive any specific grant from funding agencies in the public, commercial, or not-for-profit sectors.

References

1 K. Krishnamoorthy, M. Veerapandian, K. Yun and S. J. Kim, *Colloids Surf., B*, 2013, **112**, 521–524.
2 K. Krishnamoorthy, M. Premanathan, M. Veerapandian and S. Jae Kim, *Nanotechnology*, 2014, **25**, 315101.
3 M. I. Anik, M. K. Hossain, I. Hossain, A. M. U. B. Mahfuz, M. T. Rahman and I. Ahmed, *Nano Sel.*, 2021, **2**, 1146–1186.
4 M. Moritz and M. Geszke-Moritz, *Chem. Eng. J.*, 2013, **228**, 596–613.
5 S. Khan and M. K. Hossain, in *Nanoparticle-Based Polymer Composites*, Elsevier, 2022, pp. 15–54.
6 M. I. Anik, M. K. Hossain, I. Hossain, I. Ahmed and R. M. Doha, in *Magnetic Nanoparticle-Based Hybrid Materials*, Elsevier, 2021, pp. 463–497.
7 N. Mahmud, M. I. Anik, M. K. Hossain, M. I. Khan, S. Uddin, M. Ashrafuzzaman and M. M. Rahaman, *ACS Appl. Bio Mater.*, 2022, **5**, 2431–2460.
8 R. D. Holtz, B. A. Lima, A. G. Souza Filho, M. Brocchi and O. L. Alves, *Nanomedicine*, 2012, **8**, 935–940.
9 K. R. Raghupathi, R. T. Koodali and A. C. Manna, *Langmuir*, 2011, **27**, 4020–4028.
10 S. O. Ali Ahmad, M. Ikram, M. Imran, S. Naz, A. Ul-Hamid, A. Haider, A. Shahzadi and J. Haider, *RSC Adv.*, 2021, **11**, 23330–23344.
11 U. Qumar, M. Ikram, M. Imran, A. Haider, A. Ul-Hamid, J. Haider, K. N. Riaz and S. Ali, *Dalton Trans.*, 2020, **49**, 5362–5377.
12 Y.-N. Chang, M. Zhang, L. Xia, J. Zhang and G. Xing, *Materials*, 2012, **5**, 2850–2871.
13 A. M. Allahverdiyev, E. S. Abamor, M. Bagirova and M. Rafailovich, *Future Microbiol.*, 2011, **6**, 933–940.
14 R. Kumar, A. Umar, G. Kumar and H. S. Nalwa, *Ceram. Int.*, 2017, **43**, 3940–3961.
15 A. Sirelkhatim, S. Mahmud, A. Seeni, N. H. M. Kaus, L. C. Ann, S. K. M. Bakhori, H. Hasan and D. Mohamad, *Nano-Micro Lett.*, 2015, **7**, 219–242.
16 S. M. Dizaj, F. Lotfipour, M. Barzegar-Jalali, M. H. Zarrintan and K. Adibkia, *Mater. Sci. Eng., C*, 2014, **44**, 278–284.
17 A. Bouafia and S. E. Laouini, *Mini-Rev. Org. Chem.*, 2021, **18**, 725–734.
18 S. Yadav and G. Jaiswar, *J. Chin. Chem. Soc.*, 2017, **64**, 103–116.
19 J. He, P. Xu, R. Zhou, H. Li, H. Zu, J. Zhang, Y. Qin, X. Liu and F. Wang, *Adv. Electron. Mater.*, 2022, **8**, 2100997.
20 H. Zhang, Y. Meng, L. Song, L. Luo, Y. Qin, N. Han, Z. Yang, L. Liu, J. C. Ho and F. Wang, *Nano Res.*, 2018, **11**, 1227–1237.
21 T. Dietl, *Nat. Mater.*, 2010, **9**, 965–974.
22 F. Pulizzi, *Nat. Mater.*, 2010, **9**, 955–956.
23 M. K. Hossain, M. F. Pervez, M. N. H. Mia, S. Tayyaba, M. J. Uddin, R. Ahamed, R. A. Khan, M. Hoq, M. A. Khan and F. Ahmed, *Mat. Sci.*, 2017, **35**, 868–877.
24 N. H. Mia, S. M. Rana, F. Pervez, M. R. Rahman, K. Hossain, A. Al Mortuza, M. K. Basher and M. Hoq, *Mat. Sci.*, 2017, **35**, 501–510.
25 M. T. Rahman, M. A. Hoque, G. T. Rahman, M. M. Azmi, M. A. Gafur, R. A. Khan and M. K. Hossain, *Radiat. Eff. Defects Solids*, 2019, **174**, 480–493.
26 M. N. H. Mia, U. Habiba, M. F. Pervez, H. Kabir, S. Nur, M. F. Hossen, S. K. Sen, M. K. Hossain, M. A. Iftekhar and M. M. Rahman, *Appl. Phys. A*, 2020, **126**, 162.
27 M. Ali, S. Sharif, S. Anjum, M. Imran, M. Ikram, M. Naz and S. Ali, *Mater. Res. Express*, 2020, **6**, 1250d5.
28 B. Choudhury, R. Verma and A. Choudhury, *RSC Adv.*, 2014, **4**, 29314.
29 A. Boukhachem, M. Mokhtari, N. Benameur, A. Ziouche, M. Martínez, P. Petkova, M. Ghamnia, A. Cobo, M. Zergoug and M. Amlouk, *Sens. Actuators, A*, 2017, **253**, 198–209.
30 O. Kamoun, A. Boukhachem, S. Alleg, B. Jeyadevan and M. Amlouk, *J. Alloys Compd.*, 2018, **741**, 847–854.
31 M. Imran, M. Ikram, A. Shahzadi, S. Dilpazir, H. Khan, I. Shahzadi, S. A. Yousaf, S. Ali, J. Geng and Y. Huang, *RSC Adv.*, 2018, **8**, 18051–18058.
32 J. Hassan, M. Ikram, A. Ul-Hamid, M. Imran, M. Aqeel and S. Ali, *Nanoscale Res. Lett.*, 2020, **15**, 75.
33 M. Nafees, M. Ikram and S. Ali, *Appl. Nanosci.*, 2017, **7**, 399–406.
34 D. Sundeep, A. Gopala Krishna, R. V. S. S. N. Ravikumar, T. Vijaya Kumar, S. Daniel Ephraim and Y. L. Pavan, *Int. Nano Lett.*, 2016, **6**, 119–128.
35 D. Xiang, C. Han, J. Zhang and W. Chen, *Sci. Rep.*, 2015, **4**, 4891.
36 A. L. F. Cauduro, R. dos Reis, G. Chen, A. K. Schmid, C. Méthivier, H.-G. Rubahn, L. Bossard-Giannesini, H. Cruguel, N. Witkowski and M. Madsen, *ACS Appl. Mater. Interfaces*, 2017, **9**, 7717–7724.
37 A. Arfaoui, S. Touihri, A. Mhamdi, A. Labidi and T. Manoubi, *Appl. Surf. Sci.*, 2015, **357**, 1089–1096.
38 A. Phuruangrat, U. Cheed-Im, T. Thongtem and S. Thongtem, *Mater. Lett.*, 2016, **173**, 158–161.
39 A. Hojabri, F. Hajakbari and A. E. Meibodi, *J. Theor. Appl. Phys.*, 2015, **9**, 67–73.
40 S. K. Sen, M. S. Manir, S. Dutta, M. H. Ali, M. N. I. Khan, M. A. Matin and M. A. Hakim, *Thin Solid Films*, 2020, **693**, 137700.
41 O. Kamoun, A. Boukhachem, M. Amlouk and S. Ammar, *J. Alloys Compd.*, 2016, **687**, 595–603.
42 S. K. Sen, U. C. Barman, M. S. Manir, P. Mondal, S. Dutta, M. Paul, M. A. M. Chowdhury and M. A. Hakim, *Adv. Nat. Sci.: Nanosci. Nanotechnol.*, 2020, **11**, 025004.
43 A. Phuruangrat, U. Cheed-Im, T. Thongtem and S. Thongtem, *Mater. Lett.*, 2016, **172**, 166–170.
44 S. Bai, C. Chen, D. Zhang, R. Luo, D. Li, A. Chen and C.-C. Liu, *Sens. Actuators, B*, 2014, **204**, 754–762.

45 Z. Li, W. Wang, Z. Zhao, X. Liu and P. Song, *RSC Adv.*, 2017, **7**, 28366–28372.
46 A. Phuruangrat, S. Thipkonglas, T. Thongtem and S. Thongtem, *Mater. Lett.*, 2017, **195**, 37–40.
47 S. Yang, Y. Liu, T. Chen, W. Jin, T. Yang, M. Cao, S. Liu, J. Zhou, G. S. Zakharova and W. Chen, *Appl. Surf. Sci.*, 2017, **393**, 377–384.
48 G. Sanal Kumar, N. Illyaskutty, S. Suresh, R. S. Sreedharan, V. U. Nayar and V. P. M. Pillai, *J. Alloys Compd.*, 2017, **698**, 215–227.
49 M. K. Hossain, M. H. Ahmed, M. I. Khan, M. S. Miah and S. Hossain, *ACS Appl. Electron. Mater.*, 2021, **3**, 4255–4283.
50 M. K. Hossain, M. I. Khan and A. El-Denglawey, *Appl. Mater. Today*, 2021, **24**, 101104.
51 M. K. Hossain, G. A. Raihan, M. A. Akbar, M. H. Kabir Rubel, M. H. Ahmed, M. I. Khan, S. Hossain, S. K. Sen, M. I. E. Jalal and A. El-Denglawey, *ACS Appl. Electron. Mater.*, 2022, **4**, 3327–3353.
52 M. K. Hossain, S. Hossain, M. H. Ahmed, M. I. Khan, N. Haque and G. A. Raihan, *ACS Appl. Electron. Mater.*, 2021, **3**, 3715–3746.
53 M. K. Hossain, M. H. K. Rubel, M. A. Akbar, M. H. Ahmed, N. Haque, M. F. Rahman, J. Hossain and K. M. Hossain, *Ceram. Int.*, 2022, **48**, 32588–32612.
54 A. Mehtab, J. Ahmed, S. M. Alshehri, Y. Mao and T. Ahmad, *Nanotechnology*, 2022, **33**, 142001.
55 P. A. Arasu and R. V. Williams, *Surf. Rev. Lett.*, 2015, **22**, 1550054.
56 A. Chithambararaj and A. C. Bose, *J. Alloys Compd.*, 2011, **509**, 8105–8110.
57 J. Ortiz-Landeros, C. Gómez-Yáñez, R. López-Juárez, I. Dávalos-Velasco and H. Pfeiffer, *J. Adv. Ceram.*, 2012, **1**, 204–220.
58 M. K. Basher, M. K. Hossain, M. J. Uddin, M. A. R. Akand and K. M. Shorowordi, *Optik*, 2018, **172**, 801–811.
59 M. K. Basher, M. K. Hossain, R. Afaz, S. Tayyaba, M. A. R. Akand, M. T. Rahman and N. M. Eman, *Results Phys.*, 2018, **10**, 205–211.
60 J. S. Chen, Y. L. Cheah, S. Madhavi and X. W. Lou, *J. Phys. Chem. C*, 2010, **114**, 8675–8678.
61 S. K. Sen, S. Dutta, M. R. Khan, M. S. Manir, S. Dutta, A. Al Mortuza, S. Razia and M. A. Hakim, *Bionanoscience*, 2019, **9**, 873–882.
62 S. K. Sen, M. A. Jalil, M. Hossain, M. S. Manir, K. Hoque, M. A. Islam and M. N. Hossain, *Mater. Today Commun.*, 2021, **27**, 102404.
63 S. K. Sen, S. Dutta, L. Paik, T. C. Paul, M. S. Manir, M. Hossain and M. N. Hossain, *J. Alloys Compd.*, 2021, **876**, 160070.
64 H. Y. He, J. Fei and J. Lu, *J. Nanostruct. Chem.*, 2015, **5**, 169–175.
65 L. Zheng, Y. Xu, D. Jin, Y. Xie, Z. Lei, X. Yang, J. Dong and X. Yi, *Chem. Mater.*, 2009, **21**, 5681–5690.
66 K. Gomathi, S. Padmanathan, A. M. Ali and A. T. Rajamanickam, *Inorg. Chem. Commun.*, 2022, **135**, 109079.
67 Y. Chen, C. Lu, L. Xu, Y. Ma, W. Hou and J.-J. Zhu, *CrystEngComm*, 2010, **12**, 3740.
68 P. Wongkrua, T. Thongtem and S. Thongtem, *J. Nanomater.*, 2013, **2013**, 1–8.
69 G. S. Zakharova, C. Täschner, V. L. Volkov, I. Hellmann, R. Klingeler, A. Leonhardt and B. Büchner, *Solid State Sci.*, 2007, **9**, 1028–1032.
70 C. D. A. Lima, J. V. B. Moura, G. S. Pinheiro, J. F. D. F. Araujo, S. B. S. Gusmão, B. C. Viana, P. T. C. Freire and C. Luz-Lima, *Ceram. Int.*, 2021, **47**, 27778–27788.
71 L. G. Pereira, L. E. B. Soledade, J. M. Ferreira, S. J. G. Lima, V. J. Fernandes, A. S. Araújo, C. A. Paskocimas, E. Longo, M. R. C. Santos, A. G. Souza and I. M. G. Santos, *J. Alloys Compd.*, 2008, **459**, 377–385.
72 Y. Muraoka, J.-C. Grenier, S. Petit and M. Pouchard, *Solid State Sci.*, 1999, **1**, 133–148.
73 M. A. Py and K. Maschke, *Physica B+C*, 1981, **105**, 370–374.
74 M. Dieterle and G. Mestl, *Phys. Chem. Chem. Phys.*, 2002, **4**, 822–826.
75 S. K. S. Patel, K. Dewangan and N. S. Gajbhiye, *J. Mater. Sci. Nanotechnol.*, 2015, **31**, 453–457.
76 G. Mestl, N. F. D. Verbruggen, E. Bosch and H. Knözinger, *Langmuir*, 1996, **12**, 2961–2968.
77 G. M. Ramans, J. V. Gabrusenoks, A. R. Lusis and A. A. Patmalnieks, *J. Non-Cryst. Solids*, 1987, **90**, 637–640.
78 M. Vila, C. Díaz-Guerra, D. Jerez, K. Lorenz, J. Piqueras and E. Alves, *J. Phys. D: Appl. Phys.*, 2014, **47**, 355105.
79 A. Chithambararaj, N. S. S. S. Sanjini, A. C. C. C. Bose and S. Velmathi, *Catal. Sci. Technol.*, 2013, **3**, 1405.
80 A. Chithambararaj, D. Bhagya Mathi, N. Rajeswari Yogamalar and A. Chandra Bose, *Mater. Res. Express*, 2015, **2**, 055004.
81 S. K. Sen, M. Noor, M. A. Al Mamun, M. S. Manir, M. A. Matin, M. A. Hakim, S. Nur and S. Dutta, *Opt. Quantum Electron.*, 2019, **51**, 82.
82 J. Okumu, F. Koerfer, C. Salinga, T. P. Pedersen and M. Wuttig, *Thin Solid Films*, 2006, **515**, 1327–1333.
83 V. Madhavi, P. Kondaiah, S. S. Rayudu, O. M. Hussain and S. Uthanna, *Mater. Express*, 2013, **3**, 135–143.
84 A. Arunachalam, S. Dhanapandian, C. Manoharan and G. Sivakumar, *Spectrochim. Acta, Part A*, 2015, **138**, 105–112.
85 E. Ghaleghafi and M. B. Rahmani, *Solid State Sci.*, 2019, **94**, 85–91.
86 M. H. K. Rubel and M. K. Hossain, in *Fundamentals of Low Dimensional Magnets*, CRC Press, Boca Raton, 2022, pp. 183–205.
87 N. Benameur, A. Boukhachem, M. Ghamnia, M. A. Chakhoum, M. A. Dahamni and C. Fauquet, *Int. J. Chem. Eng. Appl.*, 2019, **10**, 33–39.
88 H. Ueda, N. Todo and M. Kurita, *J. Less-Common Met.*, 1974, **36**, 387–394.
89 A. Agarwal, S. Khasa, V. P. Seth, S. Sanghi and M. Arora, *J. Mol. Struct.*, 2014, **1060**, 182–190.
90 K. Badreddine, I. Kazah, M. Rekaby and R. Awad, *J. Nanomater.*, 2018, **2018**, 1–11.

91 K. S. Siddiqi, A. ur Rahman, Tajuddin and A. Husen, *Nanoscale Res. Lett.*, 2018, **13**, 141.
92 A. Azam, *Int. J. Nanomed.*, 2012, 3527.
93 G. A. Martínez-Castañón, N. Niño-Martínez, F. Martínez-Gutierrez, J. R. Martínez-Mendoza and F. Ruiz, *J. Nanopart. Res.*, 2008, **10**, 1343–1348.
94 H. Li, Q. Cui, B. Feng, J. Wang, X. Lu and J. Weng, *Appl. Surf. Sci.*, 2013, **284**, 179–183.
95 A. N. P. Raj, R. B. Bennie, G. A. I. Xavier, C. Joel, D. A. Chelliah and S. H. Kengaram, *J. Cluster Sci.*, 2022, **33**, 2429–2441.
96 Z. N. Kayani, M. Sahar, S. Riaz, S. Naseem and Z. Saddiqe, *Opt. Mater.*, 2020, **108**, 110457.
97 N. Rajiv Chandar, S. Agilan, R. Thangarasu, N. Muthukumarasamy, J. Chandrasekaran, S. Arunachalam and S. R. Akshaya, *J. Sol-Gel Sci. Technol.*, 2021, **100**, 451–465.
98 M. I. Anik, N. Mahmud, A. Al Masud, M. I. Khan, M. N. Islam, S. Uddin and M. K. Hossain, *ACS Appl. Bio Mater.*, 2022, **5**, 4028–4054.
99 A. Robert Xavier, A. T. Ravichandran, K. Ravichandran, S. Mantha and D. Ravinder, *J. Mater. Sci.: Mater. Electron.*, 2016, **27**, 11182–11187.
100 E. R. Weiner, *Applications of Environmental Chemistry*, CRC Press, 2010.
101 Q. Han, X. Wang, X. Liu, Y. Zhang, S. Cai, C. Qi, C. Wang and R. Yang, *J. Colloid Interface Sci.*, 2019, **539**, 575–584.